ORIGINAL PAPER

Polyantimonic acid-based materials evaluated as moisture sensors at ambient temperature

Sofia Mendes[1] · Olga Kurapova[2] · Pedro Faia[1] · Vasily Pazheltsev[2] · Artem Zaripov[2] · Vladimir Konakov[3]

Abstract

Humidity sensors are in high demand for many applications, such as environmental monitoring and air and food quality control. Despite many inorganic and organic materials exhibit moisture sensing properties, the electrical response of many existing sensors is not stable along the time. Polyantimonic acid (PAA) is characterized by elevated proton conductivity and by high thermal stability: consequently, it is seen as promising proton conductor for usage in humidity sensing devices. In this work, for the first time, PAA-based bulk solid membranes were produced and tested as potential materials for relative humidity (RH) detection and their moisture sensitivity was evaluated. Two different amounts of binder were used for moulding the solid sensors: the ones with 10% of binder were designated as 90PAA, while the ones with 20% were named 80PAA. The structures of the solid samples were investigated by X-ray diffraction (XRD) technique, adsorption–desorption curves via Brunauer–Emmett–Teller (BET), scanning electron microscopy (SEM) and energy-dispersive spectroscopy (EDS) techniques. The electrical behaviour was examined at ambient temperature by electrical impedance spectroscopy in the entire relative humidity (RH) interval (0–100%) and in the frequency range of 40 Hz up to 60 MHz. Electrical response of the materials was correlated with the structural features of the membranes. Both 90PAA and 80PAA sensors showed total resistance 3×10^5 and 3.5×10^5 Ω at 10% RH, respectively. A linear decrease of the resistance on RH was observed in the range 30–90% RH for both sensors. The electrical response of the evaluated PAA-based sensors displays good repeatability and reproducibility: the ones with lower binder content showed higher moisture sensitivity as well as very good time stability over 1 year.

Keywords Humidity sensing · Impedance spectroscopy · Polyantimonic acid-based sensors · Ionic conductivity · Binder effect · Model circuit

Highlights
- PAA-based sensors show resistance of 3×105 ohm at 10% RH and no hysteresis.
- Sensors exhibit n-type conduction behaviour at high RH.
- The electrical response of the lowest binder content sensor is stable with respect to the time.

✉ Pedro Faia
faia@deec.uc.pt

1   CEMMPRE – Electrical and Computer Engineering Department, Pinhal de Marrocos, FCTUC, University of Coimbra, Polo 2, 3030-290 Coimbra, Portugal

2   Saint Petersburg State University, Universitetskya Nab. 7/9, 199034 St Petersburg, Russia

3   Peter the Great St. Petersburg Polytechnic University, 195251 St. Petersburg, Russia

Introduction

Humidity sensors are in high demand for many applications, such as environmental monitoring, air and food quality control and medical sector [1]. Despite many efforts made, in situ humidity measurements with high sensitivity and in the full humidity range remain an unsolved problem. Relative humidity (RH) value is usually used as an environmental measuring parameter in humidity applications. The requirements for materials that make them suitable for moisture measurement, and consequently, for use in humidity sensors, were listed by Kamekichi and Tatsumi [2], and are, primarily, high sensitivity, fast response time, long-term durability, reproducibility, low cost, low hysteresis loop and operation over a wide range of RH and temperatures. To date, several types of humidity sensors have been developed [3–9].

Based on the signal measured, they can be classified into electrical sensors (capacitive or resistance/impedance-type),

mechanical sensors (based on strain-effects and mass-loading effects), optical sensors (based on transmission, reflection or quenching of electromagnetic waves) or integrated sensors. The humidity sensing mechanisms behind all moisture sensors are related to water vapour adsorption on the surface of the sensor, due to chemisorption (chemical adsorption) and physisorption (physical adsorption), and with capillary condensation processes along the sensing material's porous structure [1]. All listed groups of sensors have their advantages and drawbacks [10]. Among the listed types, electrical sensors are of particular interest as they allow measurements not only at room temperature conditions, but also at higher ones. Materials used in electrical humidity devices can display both electronic and/or ionic conductivity contributions to their overall electric response to moisture. The Grotthuss chain reaction mechanism contribution (free proton displacement) is of ionic nature and is one of the most relevant for many types of proton conductors [11]. Based on their noteworthy electrical response variation as a function of RH, enumerable materials have been evaluated for this purpose, such as conductive polymers [12], carbon-based materials [13], metal oxides [14] and metal oxide composites [15], in many different shapes, such as volume shaped and thick or thin films [16–18], and fabricated by diverse routes, like moulding, CVD, sputtering and electrospinning, just to mention some [1]. Several inorganic compounds, including fluorite and perovskites-based materials [19, 20], as well as some ion exchangers such as $Sb_2O_5 \cdot nH_2O$, $ZrO_2 \cdot nH_2O$, or $SnO_2 \cdot nH_2O$, also display ionic conduction [21]. Polyantimonic acid, PAA ($Sb_2O_5 \cdot nH_2O$, where $2 < n < 6$), is regarded as a potential proton conductor at low and intermediate temperatures since it displays a specific conductivity of 10^{-2} S/m; so, it can also be a promising candidate for humidity sensing applications. In its cubic pyrochlore structure, hydrated antimony oxide exists in the form of corner-sharing $(SbO_{6/2})^-$ octahedra connected in an anion skeleton, carrying an excess of negative charge [22]. This charge is compensated by a H^+ proton or by an oxonium ion, H_3O^+, or even by any of the exchangeable cations (Na^+, Sr^{2+}, Ag^+ etc.). Here, protons are displaced along the hydrogen bonds from one water molecule (oxonium ion) to another, in certain crystallographic positions in the PAA structure. The ion exchange and electrical properties of PAA significantly depend on the synthesis approach used [22–24]. For instance, Yu et al. [23, 24] obtained super soluble amorphous antimonic acid via controlled hydrolysis of $SbCl_3$ that was previously oxidized to $SbCl_5$; then, using 30% of hydrogen peroxide, they performed an efficient removal of Bi(III) from the solution. Hydrated antimony pentoxide was obtained also by the research group of Klestchov et al. [25, 26], using the same hydrolysis technique approach. The obtained precipitate was aged at 27 and then at 62 °C; after ageing, its thermolysis process was scrutinized in detail. Yaroshenko and Burmistrov [27, 28] investigated the electrical properties of PAA powder placed between a pair of electrodes. PAA samples had high resistance, and an electrical comportment close to dielectric behaviour (about 0.5 MΩ).

Despite its advantages, PAA cannot be shaped into the bulk form without the use of a binder. No need for thermal treatment during shaping makes PAA very attractive for sensing applications, once the fabrication costs are reduced when compared with the commonly used fabrication processes [1]; so, the choice of the binder and the amounts used are key factors. In the literature, there are reports about the use of polyvinyl alcohol (PVA) [28] and polysulfone (PSF) [29], among others, as binders for PAA-based shaped solids (SS) compaction. In a recent work by the authors [30], crystalline PAA was successfully obtained using controlled hydrolysis of $SbCl_5$ and dense PAA-based SS were fabricated using fluoroplastic as a binder. Thermal, phase stability and electrical response of the fabricated SS were investigated.

As stated, PAA is a good proton conductor [31, 32]. Despite the material is highly insoluble, high value of the dissociation constant of PAA ensures high proton conductivity of the material. It can be realized both by the surface, and the material bulk (hexagonal channels in the structure). So the mechanism is considerably different from the other oxide materials used for sensing as ZnO, TiO_2 and SnO_2 being p-n type conductors. The presence of a proton in the structure of PAA should enable fast and stable response to humidity. Besides, regardless of the amount of water content, PAA-based materials display good mechanical and thermal stability [32, 33] up to 300 °C. So, considering previous published works, including authors ones, led to the decision of considering PAA has a promising candidate for moisture sensing applications. Besides, and as far as the authors are aware, no mentions to the evaluation of PAA SS samples for moisture sensing were found in literature. So, the main objective of the present work was to evaluate PAA material as a candidate for future use in humidity sensing devices. In accordance with that main goal, in the present work, the authors investigated binder content influence on the structure and on the electrical response, due to moisture concentration, of bulky PAA-fabricated samples. Amounts of 10 and 20 wt.% of the inert fluoroplastic binder were used to fabricate the bulky samples, making certain that direct contact between particles was assured. The equivalent circuit model describing the material electrical conductivity behaviour with moisture concentration variation was developed, and allowed for a better interpretation and correlation of the conduction mechanisms present, due to RH variations, with the found microstructure of the PAA SS samples. All the obtained sensors showed n-type conduction along the full RH range, but with a sensitivity that depended on the binder percentage content.

Materials and methods

PAA-based sensor samples fabrication

The fabrication process of the bulk SS pellets that were evaluated for humidity sensing was described elsewhere [30]; nevertheless, and for ease of comprehension, it is resumed here. Crystalline PAA powder was synthesized via controlled aqueous hydrolysis of $SbCl_5$ (Acros Organics, 99%, anhydrous, Belgium, CAS 7647–18-9). Firstly, 130 ml of hydrated antimony (V) pentachloride was dropwise added to a large amount of water (5–10 l of distilled water), under intensive stirring. The obtained precipitated product was kept under the mother solution at room conditions for at least 1 week, allowing for the completion of crystallization and ageing processes. The resulting precipitate product was subsequently filtered, washed with distilled water and dried at 80 °C for 24 h. The dried hydrolysed product was then treated with an 1 M HCl solution (Lenreactiv, chemically pure, Russia), to ensure that the protonated form of PAA was obtained, and after, washed with distilled water. By last, the obtained crystalline polyantimonic acid was dried at 100 °C until a constant and unchanged weight was obtained. The crystalline PAA particles were then compacted using a fluoroplastic binder (grade F-23), an inert non-conductive binder. Two compositions were prepared, with PAA/binder ratios of 90:10 and 80:20 wt.%, and named respectively 90PAA and 80PAA. The weighted amount of fluoroplastic was dissolved in acetone (Lenreactiv, chemically pure, Russia) and mechanically mixed with the PAA powder. Cylindrical samples with diameter of 10 mm and thickness of 4 mm were obtained via cold uniaxial pressing (10 min, pressure 980 MPa), at room temperature.

Structure characterization of samples

Morphologies of the shaped samples and uncompressed powder were analysed by high-resolution scanning electron microscopy (HR-SEM, Zeiss Merlin, accelerating voltage 20 kV). The chemical composition of the samples was determined by X-ray energy-dispersive spectroscopy (EDS) (Oxford Instruments INCAx-act X-ray microanalysis spectrometer). Elemental maps were obtained for the following elements: Sb, O and F. Sample phase composition (powder and bulk membranes) was analysed by means of X-ray diffraction analysis (XRD) (diffractometer Rigaku "Ultima IV", using nickel Kα irradiation). Specific surface of PAA powder was measured using an apparatus employing Brunauer–Emmett–Teller (BET) theory (ASAP 2020MP, Micromeritics), while mercury porosimetry was used to determine the porosity distribution of the samples (AutoPore IV, model 9500, Micrometrics, in the range of 0.5 to 31.000 absolute psi).

Electrical response measurements

Complex impedance spectroscopy (CIS) (Agilent 4294A) was used to evaluate the electrical response of the samples to moisture changes, in the frequency range of 40 Hz–60 MHz, by placing the samples in a support equipped with measuring contacts, inside a closed chamber which possess a volume of approximately 6.5 l (see Fig. S1 of the supplementary material). The measurements were performed at room temperature by varying the relative humidity (RH), from dry air, i.e. 0% RH, to fully humidified air, 100% RH. The different values of RH were obtained by mixing, in the chosen ratio, water-saturated air, obtained by bubbling synthetic air through water in a bubbler, with dry synthetic air. The volumetric flow rates of both saturated wet and dry air were controlled by independent mass flow controllers, and then joined together in a mixer before passing tangentially over the surface of the sensors placed inside the test chamber (see Fig. S1 of the supplementary material). The RH percentage concentrations were checked and validated by means of gas chromatography technique using a gas chromatograph (GC) (GC1000, DANI). The temperature inside the chamber was electronically controlled with an accuracy greater than 1 °C and maintained at 25 °C (ambient temperature). The temperature was measured by means of a type K thermocouple, inserted in the same support were where fixed the heating elements (the support already mentioned, were samples were placed for the electrical measurements), being the control performed using a GEFRAN controller, model 1000, running Proportional Integrative Derivative, PID, algorithm.

Once the measuring chamber possessed a volume of around 6.5 l, to assure that the content of it was fully renovated after some time, an air flow feed rate of 5 l/h of each desired mixture was maintained for at least 90 min. Along the refilling of the test chamber, the RH mixture was checked several times, and only when it was stable and in accordance with the desired RH percentage under evaluation, the electrical measures were made. For performing the measures, a pair of gold electrodes was printed using a mask onto the extremities of the upper surface of each solid SS sample, using gold ink from Gwent Group (Gold Polymer Electrode Paste C2041206P2), and heated afterwards up to 80 °C, for 60 min. The complex impedance data integrity validation was ensured by the Agilent equipment, since it has inbuilt Kramers-Krönig transformations. For each sample type, two specimens of each composition were characterized, for which three acquisition runs were performed for each RH percentage measure: the data displayed are always the mean values of the three runs for both specimens and for each measure.

Fig. 1 XRD patterns of PAA powder, 90PAA and 80PAA materials
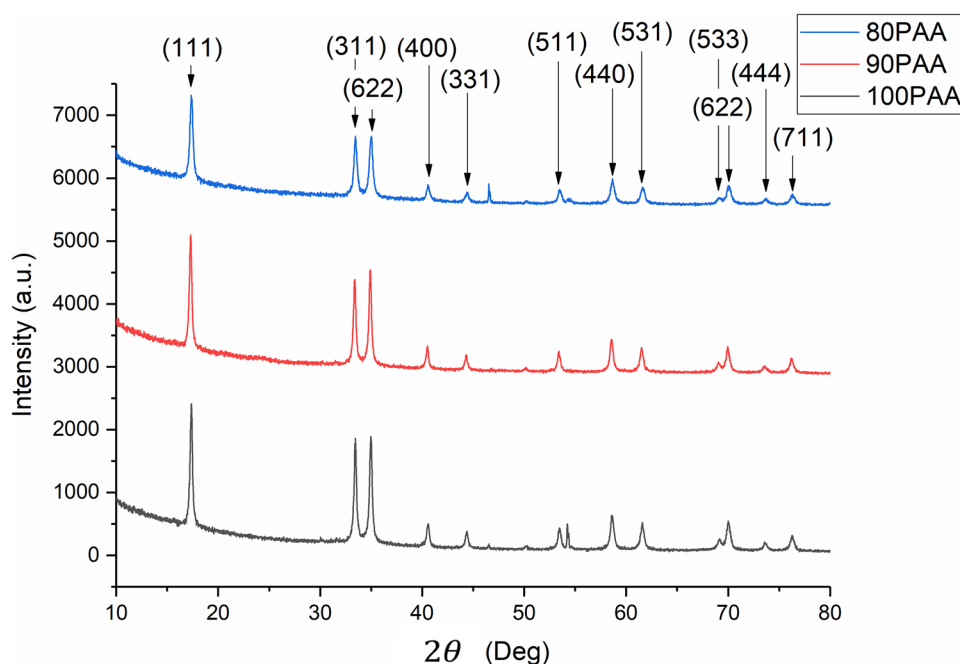
Results

Structural evaluation

A detailed structural analysis of the PAA powder with temperature increase up to 300 °C has been already carried elsewhere [30]. Based on obtained XRD data, it was shown that PAA powder after synthesis is a high crystalline compound with pyrochlore-type structure. Simultaneously, using thermal analysis (STA), the composition of PAA was calculated and found to be $Sb_2O_5 \cdot 3H_2O$. Using Raman spectroscopy, it was demonstrated that in the structure of PAA, the Sb–O polymeric chain vibrations are dominant, and ion carriers are mainly present in the form of H_3O^+ ions. However, for allowing a comprehensive discussion of the found electrical response to humidity, the structural and morphological parameters of PAA-based materials are presented here and examined. Figure 1 shows the comparison of the phase composition of pure PAA powder (100PAA), with the 90PAA and 80PAA sample materials.

As seen, the reflexes in the XRD patterns obtained for 90PAA and 80PAA materials almost coincide with the pattern for pure PAA powder. The samples' composition matches with the single-phase crystalline polyantimonic acid, $Sb_2O_5 \cdot nH_2O$ ($n = 3$–4), possessing pyrochlore-type structure of the space group $Fd\bar{3}m$. Reflexes of low intensity are present at $2\theta = 47°$ and $2\theta = 54°$ in all XRD patterns because of the addition of 10 and 20 wt.% of binder. They correspond to platinum substrate, which was used for the XRD analysis (PDF card 01–071-3756). The surface morphologies of the 90PAA- and 80PAA-based materials are presented in Fig. 2. SEM images were taken for both compressed (Fig. 2a, b and d) and uncompressed samples (Fig. 2c). As seen from Fig. 2a, b, 80PAA and 90PAA samples appear to be dense, and defects, such as large pores, are apparently non-inexistent on its surface. However, close packing of particles in the agglomerate of pure PAA powder can be observed in Fig. 2c.

Spherical PAA particles that display sizes between 130 and 180 nm seem to dominate after synthesis, display sizes between 130 and 180 nm. The binder slightly changes the particles packing in the bulk solid sensors. In contrast to the close packing of particles observed for the pure PAA powder, spherical cavities of around 500–750 nm are observed in the structure of the 80PAA sample. The shapes and sizes of the cavities allow us to suppose that the binder fills up the free spaces between the particles and the agglomerates, thus facilitating fabrication of the bulky material via cold uniaxial pressing. To track the homogeneity of the samples, the elemental distribution maps were obtained for both 90PAA and 80PAA samples (see Fig. 3).

The obtained elemental maps of oxygen and antimony duplicate each other in the zones corresponding to $Sb_2O_5 \cdot 3H_2O$ powder after synthesis. Fluorine is absent in the zones where O and Sb are distributed, being allocated between them. Additionally, it is observable that fluoroplastic does not cover neither the individual particles nor the agglomerates of PAA powder: instead, it is located in the irregular cavities formed during the packing of particles and agglomerates.

Adsorption–desorption curves of PAA powder analysed by means of BET method are shown in Fig. 4. The isotherm

Fig. 2 HR-SEM images of **a** morphology of 90PAA sample, **b** morphology of 80PAA sample, **c** the morphology of pure PAA agglomerate, **d** the cleavage of the 90PAA sample
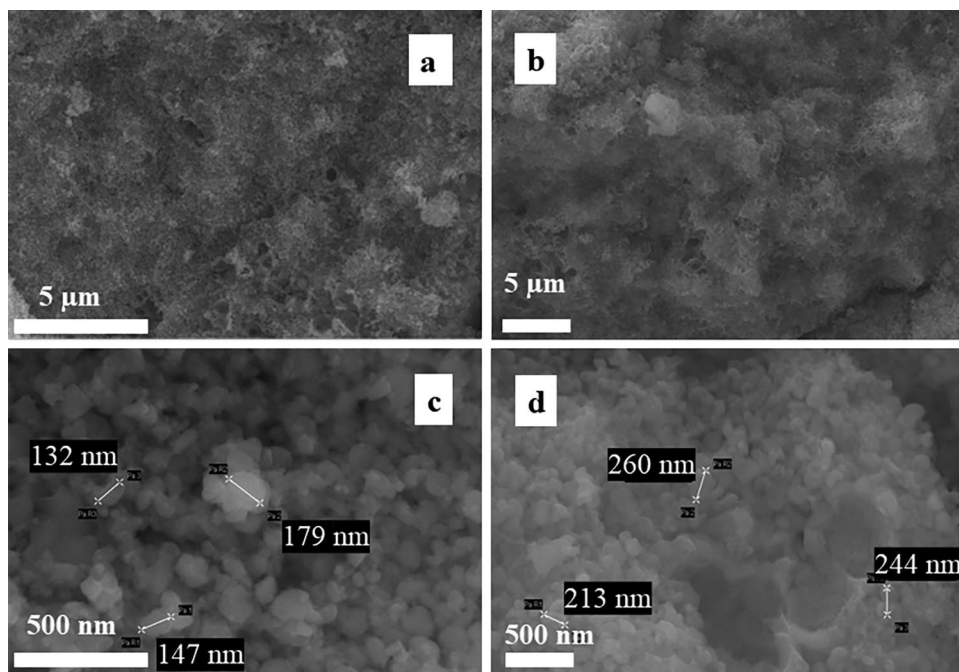

shape corresponds to type I, according to isotherm classification [34], typically observed in various mesoporous hydrated oxides. Narrow hysteresis loop in the nitrogen isotherm at high nitrogen p/p° confirms that the interparticle mesoporosity is predominant in the 100PAA sample. Indeed, the total volume of pore possessing diameters smaller than 244 nm is of 0.127 cm^3/g at relative pressure p/p° of 0.99. The specific surface area of 100PAA powder calculated from the adsorption–desorption curve is relatively low, 13.92 cm^2/g (see Table 1), but enough to allow the material to display moisture sensing properties. The obtained data on specific surface area is in accordance with recent mercury porosimetry results for 90PAA and 80PAA SS samples previously reported [30]; all presented similar pore diameters and pore volumes. However, 90PAA samples exhibited higher mean pore diameters in the mesoporous region and, as a result, a slightly higher overall contact surface area, than 80PAA sample. Since the specific surface area of the samples plays an important role in humidity sensing, one can suggest that the produced PAA-based SS may display response to humidity variations.

Moisture influence on the electrical response

Generally, the electrical response of a material to moisture depends on the moisture concentration, on peculiarities of chemisorption and physisorption of water molecules along the surface and on the material porous structure. In the

Fig. 3 EDX elemental maps of oxygen (O), antimony (Sb) and fluorine (F) obtained for cleavage of 90PAA sample (**a**–**c**); and for cleavage of 80PAA sample (**d**–**f**)
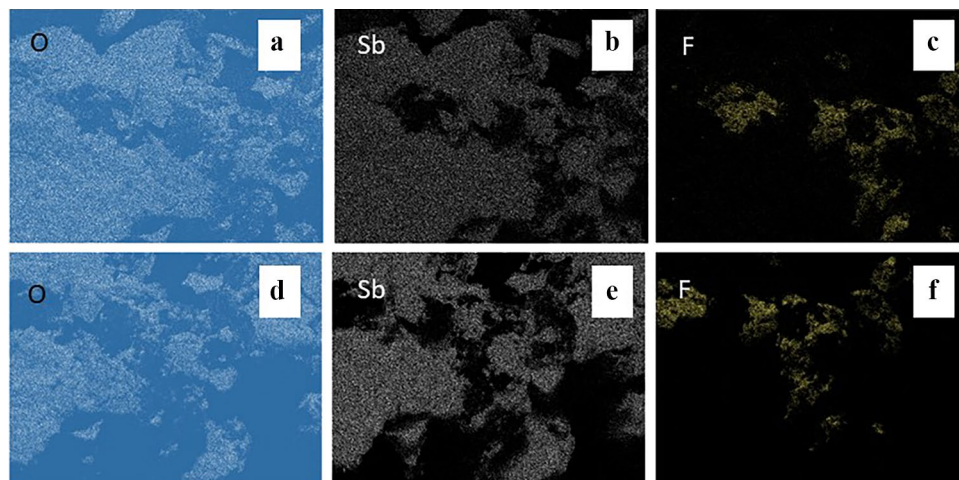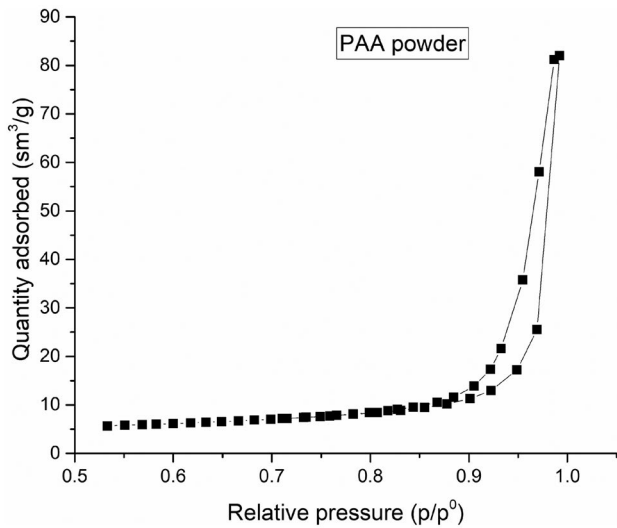
**Fig. 4** BET isotherm obtained for 100PAA powder without binder

Table 1 Samples BET and porosimetry data

|	100PAA	90PAA	80PAA
Specific surface area, cm^2/g [from BET]	13.92		
Total volume of pores with pore diameters less than 244 nm, cm^3/g	0.127		
Mean pore diameters, nm (from porosimetry data [27])		70	50

present work, the response of PAA samples to moisture was evaluated by means of CIS. The Nyquist plots obtained for both samples in the RH range 10–100%, with a step increment of 10%, are displayed in Figs. 5 and 6 (the plot at RH = 10% was recorded for 80PAA sample, but it is not displayed in the graph since it was not possible to validate moisture concentration inside the measuring chamber). By inspection of the Nyquist diagrams, it can be stated that the samples exhibit quite significant impedance variation with RH concentration. Indeed, they both display continuous decrease of the impedance with the increase of RH concentration. The observed variation of the impedance allows to suggest that PAA samples exhibit n-type electrical behaviour at low RH values. A high ionic conductivity contribution, accompanied by the visible Warburg-type component (the large straight line in the Nyquist spectra), is observed in the investigated moisture range. Warburg contribution, most likely, is originated from diffusion processes taking place along the material surface, in the interface between the solid sample and the measuring electrodes and in the pores that get filled with water.

Also, in the spectra obtained for 80PAA and 90PAA SS, a contribution composed of two semicircles is visible for all studied RH range. According to Bauerle, in the equivalent circuit for polycrystalline materials [35, 36], the small semicircle at high frequencies (see the inset in Figs. 5 and 6) is responsible for the conductivity of PAA bulk (grain and grain agglomerates), whereas a larger semicircle stands

Fig. 5 Nyquist diagrams for sample 90PAA as a function of RH. The inset represents the semicircle at high frequencies that stands for a grain conductivity of PAA
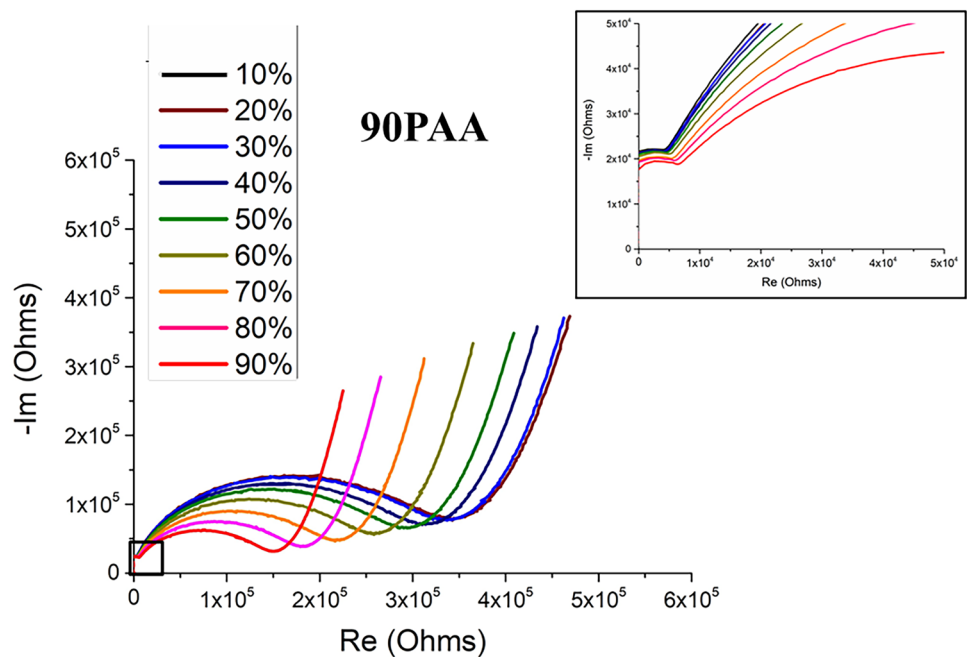
Fig. 6 Nyquist diagrams for sample 80PAA as a function of RH. The inset represents the semicircle at high frequencies that stands for a grain conductivity of PAA
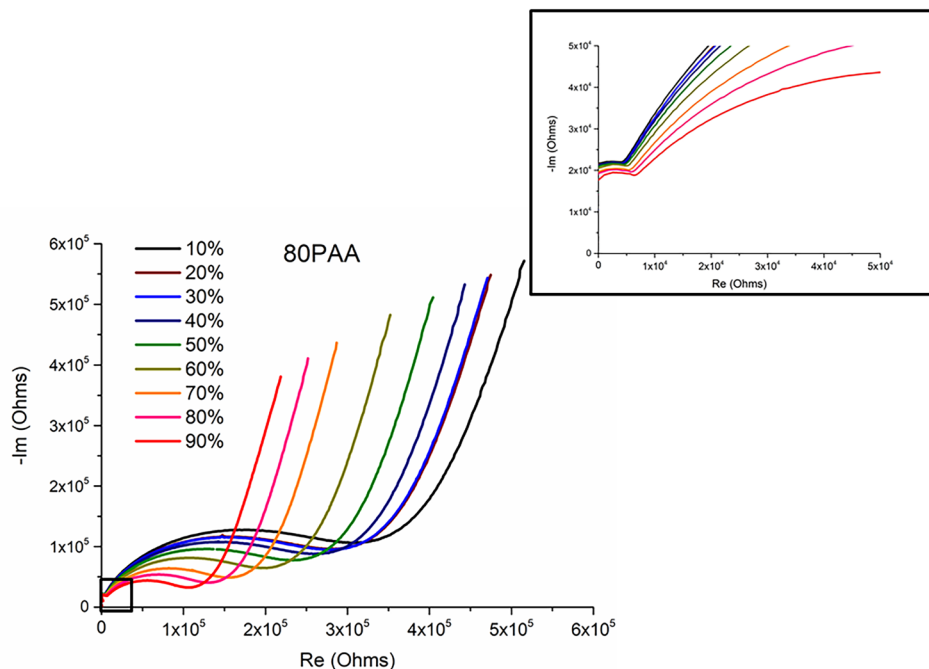
for the conductivity of grain boundaries. The fact that what seems to be a single-shaped semicircle visible at low frequencies does not mean that only one contribution is present, but that the existing ones possess relaxation frequencies with values not far apart one from each other. Since the dimension of the semicircle decreases with the RH values increase, the electronic nature phenomena also play a role in the overall electrical response. The impact of the electronic-based contribution is more evident for the lower RH concentrations, when chemisorption dominates. So, the overall electrical response of both 90PAA and 80PAA samples displays both electronic and ionic contributions, along the entire RH range; nevertheless, the ionic one dominates. Among the diverse possible contributions to the overall electrical response are observed the originated from: the grains and grain agglomerates; from the grain boundaries; and from diffusion, caused by the charge transportation along the surface of solid PAA, along the material/measuring electrode's interface and along the pores that get filled with water (all with ionic character) [18, 35]. As seen from Figs. 5 and 6, grain component contribution is nearly independent on RH concentration. Additionally, in the high humidity range (above 30–40% RH), when the first chemisorbed water layer is completed, the grain boundary component contribution for both 80PAA and 90PAA samples seems to display almost linear decreasing behaviour with RH concentration. Using the impedance data, the total resistance was calculated. The dependencies of the total resistance on the RH are shown in Fig. 7; the adjusted slopes can be well fitted by the linear dependencies with the slopes of -3266 ohms and -3285

ohms and R^2 values (regression score function) being 0.9931 and 0.9924, for the 90PAA and 80PAA, respectively.

As seen, the total resistance of PAA-based sensors shows similar trend with the RH concentration increase for both 90PAA and 80PAA samples, being their overall sensing mechanism illustrated in Fig. 8. The resistance of 90PAA is slightly lower, likely, due to smaller binder content. For the RH values in the range 10–30%, the resistance is almost independent on the RH and its value is about $3-3.5 \times 10^5$ ohms. Indeed, according to known surface
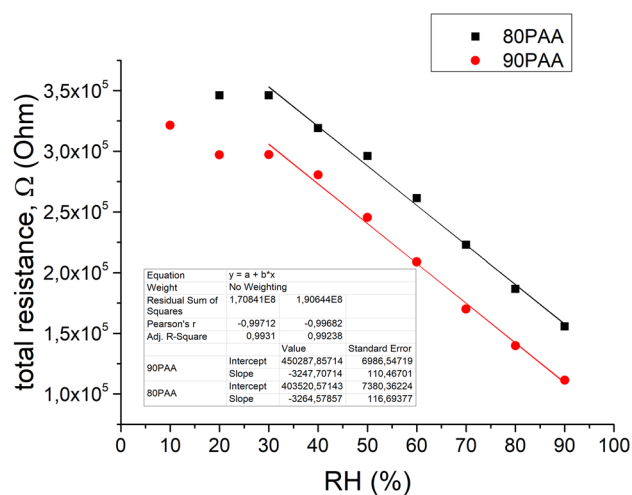
Fig. 7 The dependence of the total resistance of 80PAA and 90PAA sensors on the RH

Fig. 8 RH sensing mechanism illustration of PAA


(a)   (b)

(c)   (d)
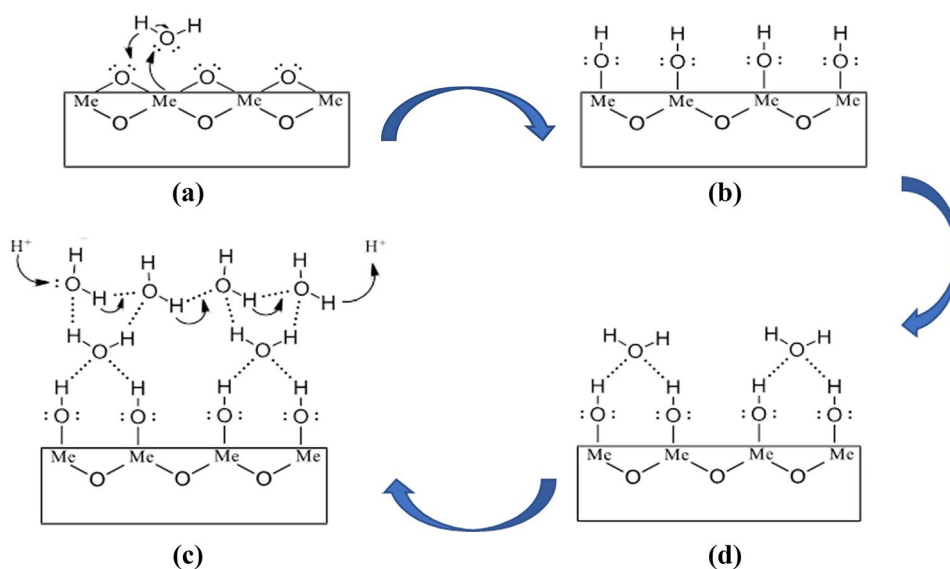
adsorption mechanisms, at low moisture concentrations, only chemisorption takes place. During the formation of the chemisorbed layer, water molecules are firmly bonded to the surface (Fig. 8a, b). The layer is complete at around RH = 30%, covering the entire surface of the material. At the same time, even at low RH, the grain component contribution is visible in the impedance spectra of both sensors. The calculated resistance of grains is about $4–6 \times 10^3$ Ω only, indicating that charge carriers (H_3O^+) start to transfer according to Grotthuss chain mechanism through the bulk of PAA $Sb_2O_5 \cdot 3H_2O$ SS already at low RH. Indeed, the protons originated from autoprotolysis of surface water molecules and/or from the distortion of O–H bonds, via the interactions with the PAA skeleton, are displaced along the hydrogen bonds from one water molecule (oxonium ion) to another one. However, at 10–20% RH, the amount of charge carriers is not enough for the effective and fast charge transfer, and the electronic contribution plays an essential role in the overall sensor response.

For RH concentrations higher than 30%, resistance values linearly decrease with moisture concentration increase, around 3.5×10^5 to 1.5×10^5 ohms for 80PAA and approximately 3×10^5 to 1×10^5 Ω for 90PAA. As already referred, not only both graphs show similar slopes, as well as R-factor, R^2, equal to 0.9983 and to 0.9924 for 80PAA and 90PAA SS, respectively. As RH concentration keeps increasing, a first physiosorbed layer forms on top of the chemisorbed one (Fig. 8c), followed by additional physiosorbed layers that get formed on top of each other. That allows to establish an effective path for charge carriers and to reach high proton conductivity in PAA-based sensor (Fig. 8d). Contrary to the chemisorbed layers, the physiosorbed ones are unstable and can be easily removed by increasing the temperature or by decreasing RH concentration [37, 38]. As the amount

of moisture concentration keeps increasing up to 90% and several physiosorbed layers are formed, saturating the material's surface, water molecules start to get condensed in the material's pore structure. When pores in the mesoporous region (pores around 10–100 nm) get totally filled with water, ion migration is enhanced once new carrier paths are established.

At the next step, a time stability evaluation was also conducted, as can be seen in Fig. 9, where the electrical response of the 90PAA sample to moisture, taken with 1-year difference, is displayed; apart from some expectable time deterioration, the sample still exhibits a very acceptable and with high similarity electrical behaviour, after 1 year time.

Indeed, and considering that the measures were taken with 1 year of interval, from a close comparison between
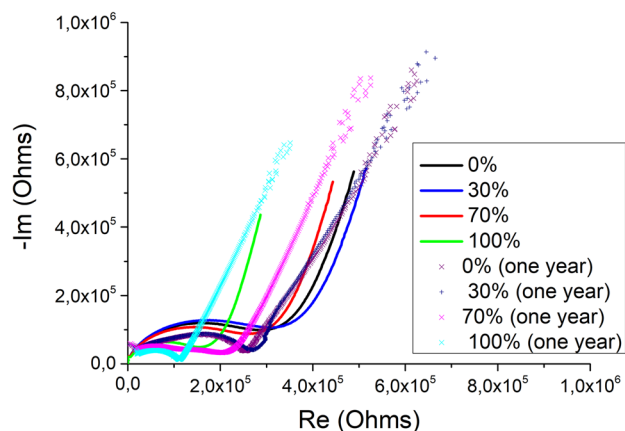
Fig. 9 Nyquist diagrams for the 90PAA taken with a 1-year time difference for different moisture concentrations (×, measures 1 year ago; −, measures at present)

the Nyquist diagrams obtained for each RH concentration, it can be stated that (1) the overall shape and trends of the Nyquist spectra show similar tendency; (2) the slopes of the main diffusion contribution to the overall electrical response, identified by the Warburg straight line, display very similar values; and (3) the samples display similar behaviour in terms of the variation of the contributions, as RH concentration increases.

Regarding the last-mentioned fact, and from the comparison of both time periods, the following similarities are seen: (1) when RH increases from 0 to 30%, insignificant differences in the electrical response are found, once the Nyquist plots do not exhibit noticeable variations; (b) when RH raises to 70 and then to 100%, variations in the Nyquist diagrams take place, but with very similar amplitudes. So, it can be concluded that the 1-year time deterioration observed is acceptable.

Hysteresis behaviour of the samples was also assessed. Hysteresis is the difference between the values obtained from two measurements, taken for the same conditions of the variable under evaluation, the first during a series of increasing measurements, while the second is obtained during a series of decreasing measurements. The maximum deviation between these two characteristic curves is named hysteresis and is expressed as a percentage of the full scale (% FS) [39]. Figure 10 shows the Nyquist diagrams and the overall impedance modulus variation obtained for 90PAA sensor in the entire tested moisture range (all obtained for ascending and descending variations). As it can be seen, 90PAA sample does not exhibit hysteretic behaviour. Indeed, in the graphs (see Fig. 8), there is a high superposition level between the traces corresponding to the measures taken for ascending and descending RH concentration variations. Consequently, in accordance with the hysteresis definition in measurements and measurement device domain, the samples do not exhibit hysteresis. This fact is of major relevance once it is better than the ones found in previously published results for hysteresis behaviour [3, 8, 40] (see Table 2). For instance, despite low resistance in all humidity range,
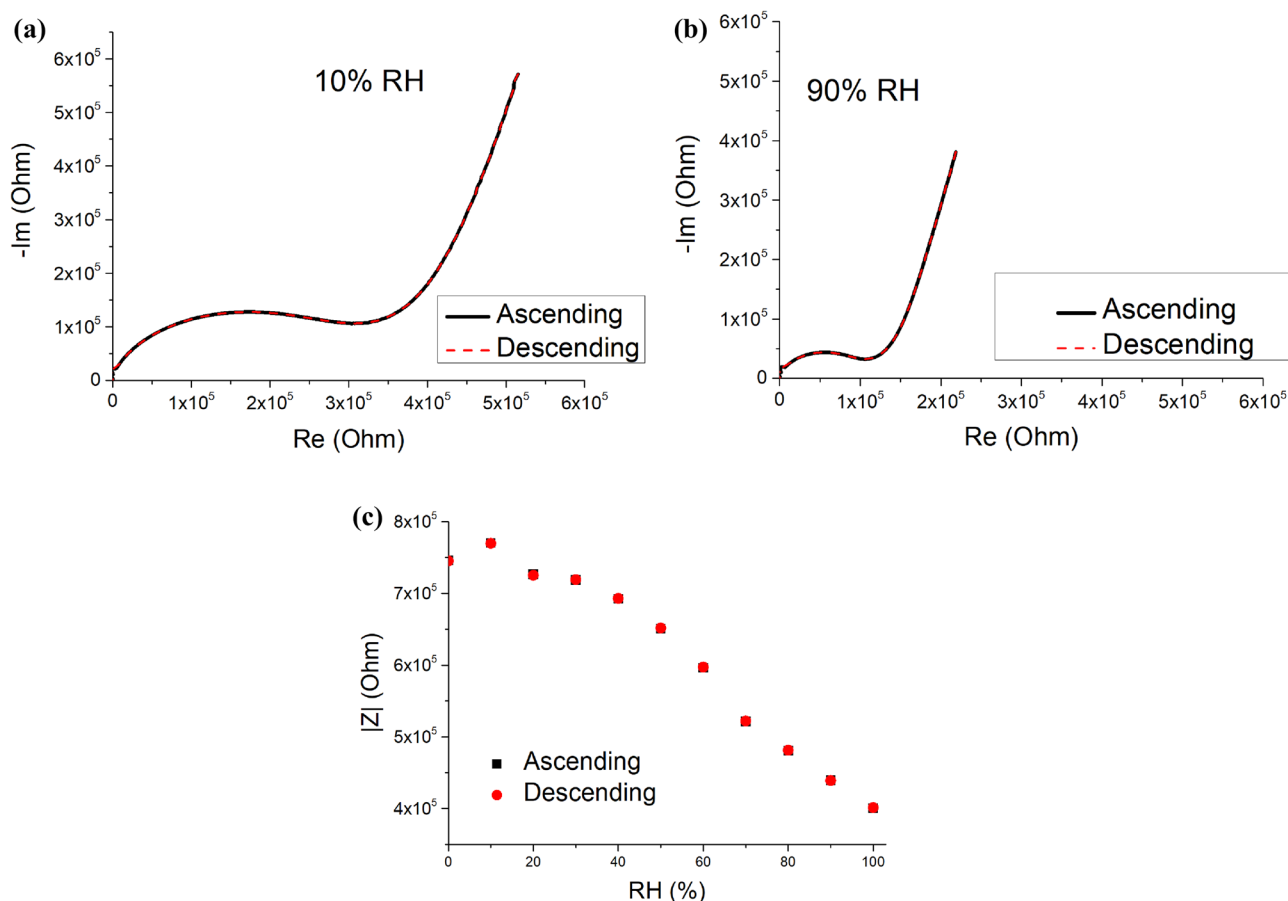

Fig. 10 Hysteresis evaluation of 90PAA sensor response to moisture for both ascending and descending RH variations: **a** for 10% RH; **b** for 90% RH; **c** along the entire RH tested range at 400 Hz

Table 2 Literature data on the resistance of some humidity sensors

Material type	Resistance (ohms)	RH value (%)	Impedance (ohms)	Hysteresis	References
$Sb_2O_5 \cdot 3H_2O$	3×10^5	10	7.3×10^5	No	Present work
	1×10^5	90	3.5×10^5 (400 Hz)		
SbSeI	-	75	1×10^5 (1 kHz)	Low (3.9%)	[8]
		30	1.15×10^6 (1 kHz)		
SnO_2	10^9	30	-	No data	[41]
	10^6	60			
	5.9×10^5	25	-	No data	[42]
	3.2×10^5	90			
ZnO/SnO_2	-	25	10^7	Yes	[40]
		90	10^4		
WS_2-modified SnO_2	195	30	-	No data	[43]
	225	90			
Porous TiO_2	-	10	$5 \times 10^5 - 10^8$	No	[44]
		90	10^4		
$Bi_6S_2O_{15}$ nanowires	5×10^5	25	-	Yes	[3]
	20	90			

$Bi_6S_2O_{15}$- and ZnO/SnO_2-based sensors show a significant hysteresis [3, 40], indicating that other processes like physisorption and chemisorption take place.

Regarding humidity sensing, comparative results of the resistance of the under discussion sensor, with data found in literature for some oxide materials, are also presented
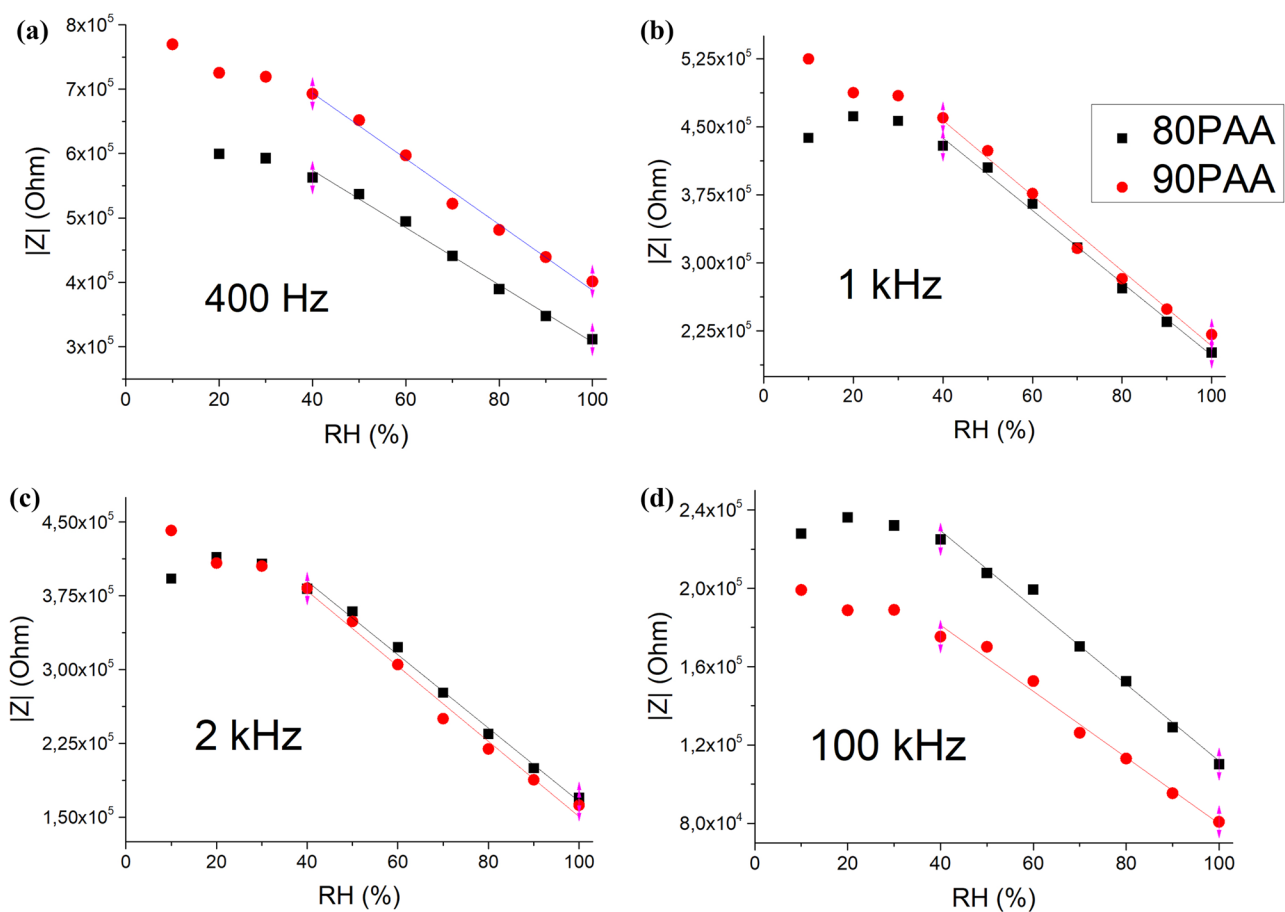
Fig. 11 Impedance modulus variation with RH concentration for both samples at 400 Hz (**a**), 1 kHz (**b**), 2 kHz (**c**) and 100 kHz (**d**), respectively

Table 3 Overall impedance modulus variation (Ohms) along the full RH range at various test frequencies

Sample	Frequency (Hz)			
	400	1000	2000	100,000
90PAA	3.69×10^5	3.04×10^5	2.79×10^5	1.18×10^5
80PAA	2.63×10^5	2.37×10^5	2.23×10^5	1.16×10^5

in Table 2. As seen from it, the resistance data obtained in the present paper slightly exceed the results obtained for SnO_2-based humidity sensor [42]. Comparing with other listed materials used in humidity sensors, PAA-based sensor shows better performance; significantly lower resistance (higher sensitivity) at low RH; and linear response to humidity in a wide RH range, 30–90%. Even though the data for WS_2-modified SnO_2 is very promising, the increase of the resistance values with RH was reported, indicating that polarization or other related phenomena took place during the measurements.

At last, to evaluate the binder concentration influence on the sample's sensitivity to moisture, plots of the impedance modulus of both sensors were computed and compared for diverse excitation frequencies (see Fig. 11). Both SS exhibit a decreasing variation of the impedance modulus with RH % increase. From the figures, it is seen that for higher frequencies, the overall impedance modulus variation decreases, and that the best operating frequency is 400 Hz. Once the sensors display a high ionic contribution to the overall electrical response, it is expectable that the highest impedance modulus variation found is located in the lower frequencies of the sweep range used in the CIS measures. This assumption was also corroborated by the computed overall impedance modulus variation over the entire RH tested range, and for the chosen frequencies, see Table 3. Besides the fact that the best sensitivity is observed for the test frequency of 400 Hz, it is also clear that the 90PAA sample displays higher sensitivity to moisture than the 80PAA one, once the overall impedance modulus variation is higher. In conclusion, the data confirm that 90PAA sensor shows better sensitivity to moisture and the most suitable test frequency is 400 Hz.

For finalizing the samples' electrical response evaluation to moisture, the authors developed using the obtained spectra an equivalent circuit model representative of their behaviour (see Fig. 12). It is known that the impedance spectra illustrate the diverse polarization and electrical phenomena that contribute to the overall response of the materials. For a certain set of data, more than one equivalent circuit can be used for fitting the obtained data with a satisfactory result. The choice between these circuits must be based both in simplicity and in consistency with the known physical and chemical phenomena taking place [35]. The proposed equivalent circuit model representing the electrical response to RH changes is similar with the suggested by authors recently [30], for representing PAA SS electrical changes with temperature variation. The initial values of the components in the model were obtained using EIS spectra analyser software, followed by their manual fine tuning. In Fig. 13, some examples of the fits performed using the proposed model are shown (additional plots can be seen in Figure S2 or the supplementary material).

From the plotted fittings, the adequacy of the studied and developed equivalent model can be confirmed; indeed, both the Nyquist and Bode fits show a high agreement with the obtained experimental data. In the proposed model, the contributions considered are the following: (1) a Warburg-type element, Warburg$_{coefficient}$, allowing for the representation of the strong ionic diffusion contribution present (the chosen Warburg element was a classic one of the semi-infinite linear types, $Z_W = \frac{W_{coef.}}{\sqrt{2\pi f}} - j\frac{W_{coef.}}{\sqrt{2\pi f}}$). This contribution is mainly due to the surface paths for charge carriers originated along the pore's surface and along pores that get filled with water, as RH increases; (2) two constant phase elements, CPE1 and CPE2, with respective pair of components ($Z_{CPE} = \frac{1}{Q}f^{-n}\left(cos\left(\frac{n\pi}{2}\right) - jsin\left(\frac{n\pi}{2}\right)\right)$), once charge diffusion contributions arising from the interface between the electrodes and the material, and along grain boundaries, due to water coverage on the materials' surface, are present (for both referred diffusion mechanisms, the interfacial character of their impedance makes it partly capacitive as well as resistive in nature); (3) one element composed of a resistor in parallel with a capacitor, R//C (representing the bulky granular and grain agglomerates contribution, $Z_{R//C} = \frac{R}{1+(2\pi f)^2C^2R^2} - j\frac{2\pi fCR}{1+(2\pi f)^2C^2R^2}$); (4) a geometric capacitance, C_{GEO} ($Z_{C_{GEO}} = -j\frac{1}{2\pi fC}$), standing for the geometric

Fig. 12 Impedance modulus variation with RH concentration for both samples at 400 Hz (**a**), 1 kHz (**b**), 2 kHz (**c**) and 100 kHz (**d**), respectively
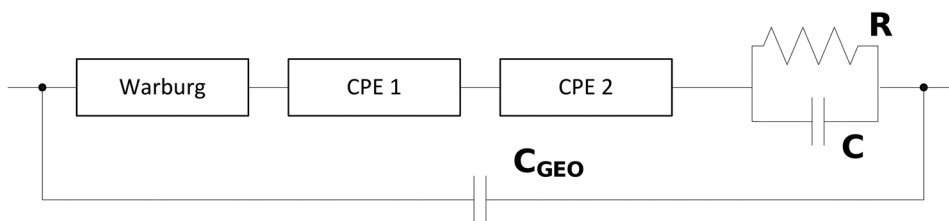
Fig. 13 Fitted experimental data using the proposed model at 10, 50 and 90% RH for both samples: **a** Nyquist diagram for sample 90PAA at 10% RH; **b**, **c** Bode diagrams for the real and imaginary components of the impedance for sample 90PAA at 10% RH; **d**, **e** Nyquist diagram for sample 80PAA at 50 and 90% RH, respectively; **f** Nyquist diagram for sample 80PAA at 10% RH; **g**, **h** Bode diagrams for the real and imaginary components of the impedance for sample 80PAA at 10% RH; **i**, **j** Nyquist diagram for sample 90PAA at 50 and 90% RH, respectively
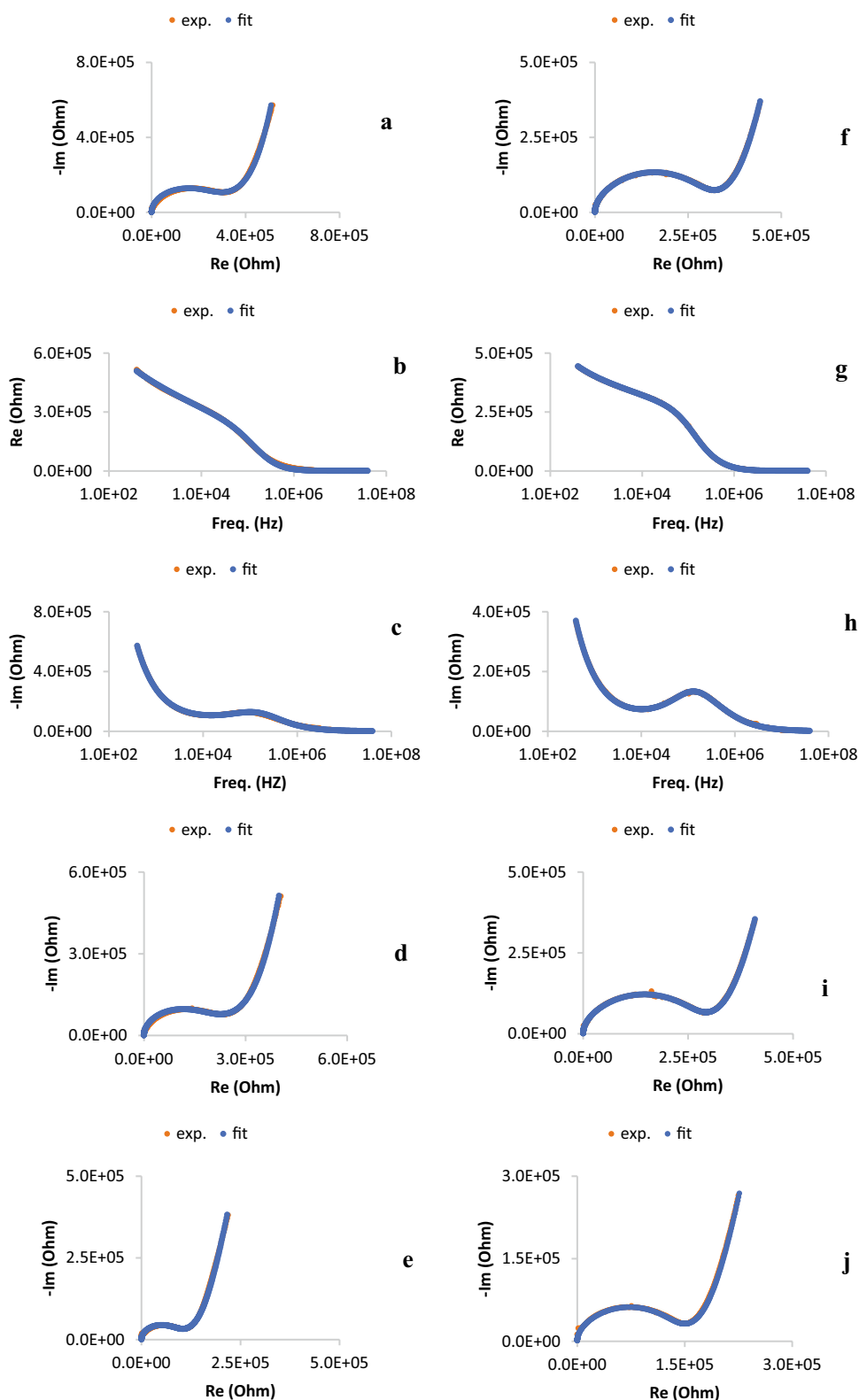
effect contribution of the electrode's location, which are placed on the extremities of the upper faces of the samples, and consequently, the measuring configuration exhibits a shape that has similarities to the one of a capacitor with parallel plates, with the under test material in-between plates.

Table 4 Fitted parameters using the proposed equivalent circuit model for sample 90PAA

RH (%)	R (Ω)	C (F)	C_{GEO} (F)	Q_{CPE1} (S×s^n)	n_{CPE1} (a.u.)	Q_{CPE2} (S×s^n)	n_{CPE2} (a.u.)	W_{coeffi} (Ω×s$^{-1/2}$)
10	$1.00\times10^{+03}$	1.30×10^{-09}	3.65×10^{-12}	9.71×10^{-10}	9.82×10^{-01}	7.39×10^{-07}	1.25×10^{-01}	2.19×10^{-12}
20	$1.00\times10^{+03}$	3.22×10^{-09}	3.33×10^{-12}	9.39×10^{-10}	9.90×10^{-01}	6.76×10^{-07}	1.42×10^{-01}	1.79×10^{-12}
30	$1.20\times10^{+03}$	8.22×10^{-09}	3.62×10^{-12}	1.03×10^{-09}	9.77×10^{-01}	8.29×10^{-07}	1.23×10^{-01}	1.66×10^{-12}
40	$1.00\times10^{+03}$	1.09×10^{-08}	3.60×10^{-12}	1.06×10^{-09}	9.76×10^{-01}	8.92×10^{-07}	1.22×10^{-01}	1.46×10^{-12}
50	$1.00\times10^{+03}$	1.19×10^{-08}	3.56×10^{-12}	1.14×10^{-09}	9.70×10^{-01}	1.01×10^{-06}	1.19×10^{-01}	1.29×10^{-12}
60	$1.00\times10^{+03}$	1.29×10^{-08}	3.51×10^{-12}	1.26×10^{-09}	9.62×10^{-01}	1.21×10^{-06}	1.17×10^{-01}	1.14×10^{-12}
70	$1.00\times10^{+03}$	1.57×10^{-08}	3.45×10^{-12}	1.47×10^{-09}	9.51×10^{-01}	1.61×10^{-06}	1.11×10^{-01}	1.25×10^{-12}
80	$1.00\times10^{+03}$	1.52×10^{-08}	3.42×10^{-12}	1.66×10^{-09}	9.42×10^{-01}	1.94×10^{-06}	1.09×10^{-01}	1.16×10^{-12}
90	$1.00\times10^{+03}$	1.72×10^{-08}	3.40×10^{-12}	1.97×10^{-09}	9.28×10^{-01}	2.44×10^{-06}	1.05×10^{-01}	1.79×10^{-12}
100	$1.00\times10^{+03}$	2.11×10^{-08}	3.39×10^{-12}	2.37×10^{-09}	9.12×10^{-01}	3.10×10^{-06}	1.01×10^{-01}	2.99×10^{-12}

The fitted parameters for samples 90PAA and 80PAA using the proposed model circuit are displayed in Tables 4 and 5, respectively. All fitted parameters exhibit a standard deviation lower than 1%. A closer look to the tables allows to conclude that:

1. The electronic nature contribution originated by the grain agglomerates, represented by the R//C element, displays an increase of one order of magnitude between the 90PAA and the 80PAA samples; this is due to the higher amount of binder content present in the 80PAA samples, which increases the separation between PAA grains and agglomerates. Nevertheless, for both types of binder content samples, the values of this circuit element contribution to the overall electrical response do not vary significantly along the full RH concentration studied range, confirming the smaller contribution from the grain and grain agglomerates to the overall electrical response of the samples.

2. The considered geometric contribution effect, C_{GEO}, originated by the measuring contact positioning, is clearly confirmed; besides, once the contribution val-

ues for both samples over the entire evaluated moisture range are quite similar, their good adhesion to the sample's surface is also a fact.

3. For both samples, the two CPE circuit elements considered display different behaviours and values regarding moisture increase; indeed, while for CPE1 element, both samples display very similar values between them along the full moisture range, the lower content sample, presents for CPE2 component as expected, and due to its lower binder content, values almost one order of magnitude lower for the lower RH concentrations, in agreement with the observed higher impedance values and overall variation with RH concentration observed for sample 90PAA.

4. The Warburg-type contribution coefficient is quite significant for both samples; however, for the higher binder content sample and for all RH concentrations, it displays higher values when compared with the lower content one, in accordance with the observed higher slope of the Warburg contribution in the spectra for that sample.

Table 5 Fitted parameters using the proposed equivalent circuit model for sample 80PAA

RH (%)	R (Ω)	C (F)	C_{GEO} (F)	Q_{CPE1} (S×s^n)	n_{CPE1} (a.u.)	Q_{CPE2} (S×s^n)	n_{CPE2} (a.u.)	W_{coeffi} (Ω×s$^{-1/2}$)
10	$6.18\times10^{+04}$	1.09×10^{-11}	2.76×10^{-12}	1.93×10^{-09}	9.44×10^{-01}	1.36×10^{-06}	9.11×10^{-01}	1.44×10^{-12}
20	$6.72\times10^{+04}$	1.06×10^{-11}	2.76×10^{-12}	1.88×10^{-09}	9.46×10^{-01}	1.27×10^{-06}	9.29×10^{-01}	7.78×10^{-12}
30	$6.65\times10^{+04}$	1.10×10^{-11}	2.77×10^{-12}	1.90×10^{-09}	9.44×10^{-01}	1.31×10^{-06}	9.15×10^{-01}	6.23×10^{-12}
40	$5.85\times10^{+04}$	1.20×10^{-11}	2.77×10^{-12}	2.06×10^{-09}	9.37×10^{-01}	1.42×10^{-06}	8.85×10^{-01}	4.05×10^{-12}
50	$5.47\times10^{+04}$	1.17×10^{-11}	2.76×10^{-12}	2.11×10^{-09}	9.37×10^{-01}	1.52×10^{-06}	$8,81\times10^{-01}$	3.51×10^{-12}
60	$5.16\times10^{+04}$	1.27×10^{-11}	2.72×10^{-12}	2.13×10^{-09}	9.40×10^{-01}	1.70×10^{-06}	9.02×10^{-01}	3.37×10^{-12}
70	$2.92\times10^{+04}$	1.85×10^{-11}	2.81×10^{-12}	2.36×10^{-09}	9.33×10^{-01}	2.07×10^{-06}	8.01×10^{-01}	1.13×10^{-11}
80	$3.17\times10^{+04}$	1.18×10^{-11}	2.71×10^{-12}	2.49×10^{-09}	9.37×10^{-01}	2.44×10^{-06}	8.47×10^{-01}	2.54×10^{-11}
90	$2.53\times10^{+04}$	1.18×10^{-11}	2.71×10^{-12}	2.69×10^{-09}	9.35×10^{-01}	2.91×10^{-06}	8.41×10^{-01}	1.85×10^{-11}
100	$2.40\times10^{+04}$	1.22×10^{-11}	3.05×10^{-12}	2.74×10^{-09}	9.41×10^{-01}	3.31×10^{-06}	9.06×10^{-01}	1.85×10^{-11}

In summary, polyantimonic acid is a very promising material, deserving to be further studied for future use in humidity sensing applications and devices: indeed its total resistance values at low humidity (3×105 Ohm at 10% RH), due to protons present in the $Sb_2O_5\cdot3H_2O$ structure, linear decrease of the resistance with RH variations from 30 to 90%. Besides, long-time acceptable deterioration and non-existing hysteresis, all combined with the low fabrication cost (much smaller than the used with traditional ceramic or polymeric used materials), allow to confirm that possibility.

Conclusions

Via XRD, SEM and EDS, it was shown that the binder fills up the free spaces between the crystalline PAA particles and particle agglomerates, thus enabling the direct transfer of proton through the bulk of PAA. Using BET method, it was confirmed that the specific surface area of 100PAA pure powder is 13.92 cm^2/g and that interparticle mesoporosity is predominant. Using electrical impedance spectroscopy, it was demonstrated that the PAA sensors exhibit linear decrease of total resistance and impedance modulus with moisture at RH = 30–90%. Both 90PAA and 80PAA sensors showed low total resistance values at low humidity (3×10^5 and 3.5×10^5 Ω at 10% RH).

The 90PAA sensor displayed no hysteresis and a very acceptable time response deterioration. So, together with a low fabrication cost, PAA displays desirable properties for humidity sensing applications such as linear response over the RH range, no hysteresis and acceptable ageing response deterioration. If in further studies, using other binders, the sensitivity results of the present work, where a fluoroplastic-type one was used, are enhanced, then PAA is confirmed to be suitable for usage in up to market humidity sensing devices, in a diversity of industrial applications.

References

1. Farahani H, Wagiran R, Hamidon MN (2014) Humidity sensors principle, mechanism, and fabrication technologies: a comprehensive review. Sensors 14:7881–7939. https://doi.org/10.3390/s140507881

2. Kamekichi S, Tatsumi T (1965) Wet and dry plate dew point hygrometer. In: Ruskin RE (ed) Humidity and moisture 1. pp 64–69

3. Zhou Y, Grunwaldt J-D, Krumeich F, Zheng K, Chen G, Stötzel J, Frahm R, Patzke GR (2010) Hydrothermal synthesis of $Bi_6S_2O_{15}$ nanowires: structural, in situ EXAFS, and humidity-sensing studies. Small 6:1173–1179. https://doi.org/10.1002/smll.201000112

4. Anisimov YA, Evitts RW, Cree DE, Wilson LD (2021) Polyaniline/biopolymer composite systems for humidity sensor applications: a review. Polymers 13:2722. https://doi.org/10.3390/polym13162722

5. Chu Y, Young S, Ding R, Chu T, Lu T, Ji L (2021) Improving ZnO nanorod humidity sensors with Pt nanoparticle adsorption. ECS J Solid State Sci Technol 10(3):037003. https://doi.org/10.1149/2162-8777/abeb53

6. Li R, Fan Y, Ma Z, Dan Z, Liu Y, Xu J (2021) Controllable preparation of ultrathin MXene nanosheets and their excellent QCM humidity sensing properties enhanced by fluoride doping. Microchim Acta 188:81. https://doi.org/10.1007/s00604-021-04723-2

7. Lu Y, Yang G, Shen Y, Yang H, Xu K (2022) Multifunctional flexible humidity sensor systems towards noncontact wearable electronics. Nano-Micro Lett 14:150. https://doi.org/10.1007/s40820-022-00895-5

8. Mistewicz K, Starczewska A, Jesionek M, Nowak M, Kozioł M, Stróż D (2020) Humidity dependent impedance characteristics of SbSeI nanowires. Appl Surf Sci 513:145859. https://doi.org/10.1016/j.apsusc.2020.145859

9. Zhang D, Zong X, Wu Z, Zhang Y (2018) Ultrahigh-performance impedance humidity sensor based on layer-by-layer self-assembled tin disulfide/titanium dioxide nanohybrid film. Sens Actuators, B Chem 266:52–62. https://doi.org/10.1016/j.snb.2018.03.007

10. Sikarwar S, Yadav BC (2015) Opto-electronic humidity sensor: a review. Sens Actuators, A 233:54–70. https://doi.org/10.1016/j.sna.2015.05.007

11. De Grotthuss CJT (1806) Sur la décomposition de l'eau et des corps qu'elle tient en dissolution à l'aide de l'électricité galvanique. Ann Chim 58:54–73

12. Morais RM, Klem MDS, Nogueira GL, Gomes TC, Alves N (2018) Low cost humidity sensor based on PANI/PEDOT:PSS Printed on Paper. IEEE Sens J 18(7):2647–2651. https://doi.org/10.1109/JSEN.2018.2803018

13. Tulliani J-M, Inserra B, Ziegler D (2019) Carbon-based materials for humidity sensing: a short review. Micromachines 10:232. https://doi.org/10.3390/mi10040232

14. McGhee JR, Sagu JS, Southee DJ, Evans PSA, Wijayantha KGU (2020) Printed, Fully metal oxide, capacitive humidity sensors

using conductive indium tin oxide inks. ACS Appl Electron Mater 2(11):3593–3600. https://doi.org/10.1021/acsaelm.0c00660

15. Zhu Z, Lin W-D, Lin Z-Y, Chuang M-H, Wu R-J, Chavali M (2021) Conductive polymer (graphene/PPy)–BiPO4 composite applications in humidity sensors. Polymers 13:2013. https://doi.org/10.3390/polym13122013

16. Najeeb MA, Ahmad Z, Shakoor RA (2018) Organic thin-film capacitive and resistive humidity sensors: a focus review. Adv Mater Interfaces 5(21):1800969. https://doi.org/10.1002/admi.201800969

17. Park SY, Lee JE, Kim YH, Kim JJ, Shim Y-S, Kim SY, Lee MH, Jang HW (2018) Room temperature humidity sensors based on rGO/MoS$_2$ hybrid composites synthesized by hydrothermal method. Sens Actuators, B Chem 258:775–782. https://doi.org/10.1016/j.snb.2017.11.176

18. Faia P, Libardi J, Louro C (2016) Effect of V$_2$O$_5$ doping on p- to n- conduction type transition of TiO$_2$:WO$_3$ composite humidity sensors. Sens Actuators, B Chem 222:952–964. https://doi.org/10.1016/j.snb.2015.09.039)

19. Malavasi L, Fisher CAJ, Islam MS (2010) Oxide-ion and proton conducting electrolyte materials for clean energy applications: structural and mechanistic features. Chem Soc Rev 39:4370. https://doi.org/10.1039/b915141a

20. Slodczyk A, Colomban P, André G, Zaafrani O, Grasset F, Lacroix O, Sala B (2012) Structural modifications induced by free protons in proton conducting perovskite zirconate membrane. Solid State Ion 225:214–218. https://doi.org/10.1016/j.ssi.2012.01.023

21. England W, Cross M, Hamnett A, Wiseman P, Goodenough J (1980) Fast proton conduction in inorganic ion-exchange compounds. Solid State Ion 1:231–249. https://doi.org/10.1016/0167-2738(80)90007-7

22. Belinskaya FA, Militsina EA (1980) Inorganic ion-exchange materials based on insoluble antimony(V) compounds. Russ Chem Rev 49:933–952. https://doi.org/10.1070/RC1980v049n10ABEH002518

23. Yu T, Zhang H, Cao H, Zheng G (2019) Understanding the enhanced removal of Bi(III) using modified crystalline antimonic acids: creation of a transitional pyrochlore-type structure and the Sb(V)-Bi(III) interaction behaviors. Chem Eng J 360:313–324. https://doi.org/10.1016/j.cej.2018.11.209

24. Yu T, Shen Y, Zhang H, Xu S, Cao H, Zheng G (2021) Efficient removal of bismuth with supersoluble amorphous antimony acids: an insight into synthesis mechanism and Sb(V)-Bi(III) interaction behaviors. Chem Eng J 420(2):127617. https://doi.org/10.1016/j.cej.2020.127617

25. Klestchov D, Burmistrov V, Sheinkma A, Pletnev R (1991) Composition and structure of phases formed in the process of hydrated antimony pentoxide thermolysis. J Solid State Chem 94(2):220–226. https://doi.org/10.1016/0022-4596(91)90186-L

26. Kovalenko LY, Yaroshenko FA, Burmistrov VA, Isaeva TN, Galimov DM (2019) Thermolysis of hydrated antimony pentoxide. Inorg Mater 55(6):586–592. https://doi.org/10.1134/S0020168519060086

27. Yaroshenko FA, Burmistrov VA (2015) Proton conductivity of polyantimonic acid studied by impedance spectroscopy in the temperature range 370–480 K. Inorg Mater 51:783–787. https://doi.org/10.1134/S0020168515080208

28. Yaroshenko FA, Burmistrov VA (2016) Dielectric losses and proton conductivity of polyantimonic acid membranes. Russ J Electrochem 52:690–693. https://doi.org/10.1134/S1023193516070193

29. Leysen R, Vermeiren P, Baestle L, Spaepen G, Vanderborre J-BH (1981) Method of preparing a membrane consisting of polyantimonic acid powder and an organic binder. Patent US 4253936

30. Kurapova OY, Faia PM, Zaripov AA, Pazheltsev VV, Glukharev AA, Konakov VG (2021) Electrochemical characterization of novel polyantimonic acid based proton conductors for low and intermediate temperature fuel cells. Appl Sci 11(24):11877. https://doi.org/10.3390/app112411877

31. Kovalenko LY, Burmistrov VA, Zakharevich DA, Kalganov DA (2021) On the mechanism of proton conductivity of polyantimonic acid. Chelyabinsk Physical and Mathematical Journal 6(1):95–111. https://doi.org/10.47475/2500-0101-2021-16108

32. Kosohin O, Matvieiev O, Linyucheva O (2022) Hydrated antimonic acid as a solid electrolyte. Materials Today: Proceedings 50:521–523. https://doi.org/10.1016/j.matpr.2021.11.307

33. Kurapova OY, Zaripov AA, Pazheltsev VV, Glukharev AG, Konakov VG (2022) Bulk solid-state polyantimonic-acid-based proton-conducting membranes. Refract Ind Ceram 1–6. https://doi.org/10.1007/s11148-022-00685-x

34. Roquerol FRJS, Rouquerol J, Sing K (1999) Adsorption by powders and solids: principles, methodology, and applications. Academic Press, London 54:15893–15899.

35. Bauerle JE (1969) Study of solid electrolyte polarization by a complex admittance method. J Phys Chem Solids 30:2657–2670. https://doi.org/10.1016/0022-3697(69)90039-0

36. Barsoukov E, Macdonald JR (2018) Impedance spectroscopy: Theory, experiment, and applications, 3rd edn. John Wiley & Sons, Inc. https://doi.org/10.1002/9781119381860

37. Zanetti SM, Rocha KO, Rodrigues JAJ, Longo E (2014) Soft-chemical synthesis, characterization and humidity sensing behavior of WO$_3$/TiO$_2$ nanopowders. Sens Actuators, B Chem 190:40–47. https://doi.org/10.1016/j.snb.2013.08.053

38. Faia PM, Libardi J (2016) Response to humidity of TiO$_2$:WO$_3$ sensors doped with V$_2$O$_5$: influence of fabrication route. Sens Actuators, B Chem 236:682–700. https://doi.org/10.1016/j.snb.2016.05.109

39. Carr JJ (1993) Sensors and circuits: sensors, transducers, & supporting circuits for electronic instrumentation measurement and control. Prentice Hall

40. Li F, Li P, Zhang H (2022) Preparation and research of a high-performance ZnO/SnO$_2$ humidity sensor. Sensors 22:293. https://doi.org/10.3390/s22010293

41. Kiasari NM, Soltanian S, Gholamkhass B, Servati P (2012) Room temperature ultra-sensitive resistive humidity sensor based on single zinc oxide nanowire. Sens Actuators, A 182:101–105. https://doi.org/10.1016/j.sna.2012.05.041

42. Chang S, Chang S, Lu C, Li M, Hsu C, Chiou Y, Hsueh T, Chen I (2010) A ZnO nanowire-based humidity sensor. Superlattices Microstruct 47(6):772–778. https://doi.org/10.1016/j.spmi.2010.03.006

43. Chen Y, Pei Y, Jiang Z, Shi Z, Xu J, Wu D, Xu T, Tian Y, Wang X, Li X (2018) Humidity sensing properties of the hydrothermally synthesized WS$_2$-modified SnO$_2$ hybrid nanocomposite. Appl Surf Sci 447:325–330. https://doi.org/10.1016/j.apsusc.2018.03.154

44. Wang Z, Shi L, Wu F, Yuan S, Zhao Y, Zhang M (2011) The sol–gel template synthesis of porous TiO$_2$ for a high performance humidity sensor. Nanotechnology 22(27):275502. https://doi.org/10.1088/0957-4484/22/27/275502